# Transient Structures and Possible Limits of Data Recording in Phase-Change Materials

Jianbo Hu, Giovanni M. Vanacore, Zhe Yang,[†] Xiangshui Miao,[†] and Ahmed H. Zewail[*]

Physical Biology Center for Ultrafast Science and Technology, Arthur Amos Noyes Laboratory of Chemical Physics, California Institute of Technology, Pasadena, California 91125, United States. [†]Present address: Wuhan National Laboratory for Optoelectronics, Huazhong University of Science and Technology, Wuhan 430074, China.

ABSTRACT Phase-change materials (PCMs) represent the leading candidates for universal data storage devices, which exploit the large difference in the physical properties of their transitional lattice structures. On a nanoscale, it is fundamental to determine their performance, which is ultimately controlled by the speed limit of transformation among the different structures involved. Here, we report observation with atomic-scale resolution of transient structures of nanofilms of crystalline germanium telluride, a prototypical PCM, using ultrafast electron crystallography. A nonthermal transformation from the initial rhombohedral phase to the cubic structure was found to occur in 12 ps. On a much longer time scale, hundreds of picoseconds, equilibrium heating of the nanofilm is reached, driving the system toward amorphization, provided that high excitation energy is invoked. These results elucidate the elementary steps defining the structural pathway in the transformation of crystalline-to-amorphous phase transitions and describe the essential atomic motions involved when driven by an ultrafast excitation. The establishment of the time scales of the different transient structures, as reported here, permits determination of the possible limit of performance, which is crucial for high-speed recording applications of PCMs.
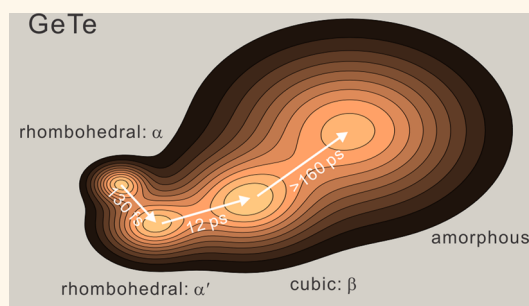
KEYWORDS: phase-change materials · ultrafast electron diffraction · phase transitions · structural dynamics · germanium telluride · Ge−Sb−Te alloy

P hase-change materials (PCMs) are the most promising candidates to be used as active media in universal data storage devices. This is because of their nonvolatility, high operating speed, scalability, and cyclability, as clearly shown for Ge−Sb−Te (GST) alloys.[1−4] Unlike the current commercial devices, where electrical charges are used for encoding the information during data storage, PCMs exploit the large difference in physical properties exhibited by their multiple structural phases.[2] As a consequence, the risk of data leakage does not practically exist, enabling a large increase of the storage density.[5−7] Demonstration of a fully functional memory with a 5 nm thick storage medium (∼8 unit cells) was recently reported.[5] However, in order to fully exploit this potential, knowledge and control of PCMs ultimate performance becomes essential, especially when the length scale reaches that of nanodevices.

Optical PCM-based devices, such as DVD and Blu-ray disc,[3] are operated by laser pulses (see illustration in Figure 1a). The recording process employs a short and intense pulse, which is able to amorphize the active medium from its initial crystalline phase. A long and relatively weak pulse is then used to recrystallize the amorphous phase in order to erase the written information. The two structurally different states, crystalline and amorphous, have distinct optical reflectivity that is enough to be exploited for data storage. Although nanosecond laser pulses are commonly used for this operation, significant effort has been devoted to explore the upper limit of the operation speed by using shorter laser pulses.[8−10] The use of femtosecond or picosecond pulses, especially during the recording process, has an intrinsic advantage over nanosecond lasers because of their efficient excitation and thus the expected enhanced rate of amorphization.

The ultimate speed of the operation is controlled by the microscopic structural dynamics, whose nature at an atomic scale
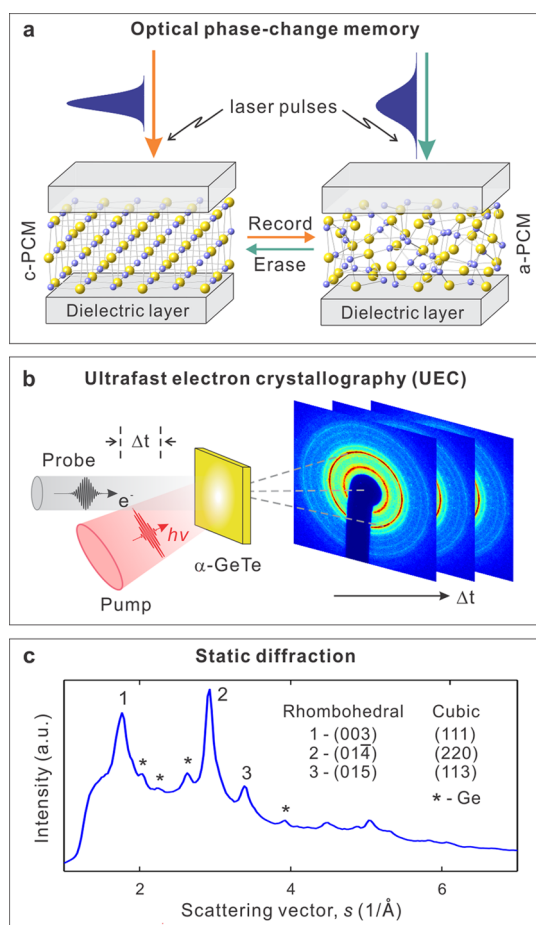
Figure 1. Phase change materials (PCMs) device, the approach (UEC), and static diffraction. (a) Representation of the writing (left) and erasing (right) operations in an optical storage material based on its phase change: c-PCM and a-PCM are the crystalline and amorphous phases, respectively. (b) Representation of the layout for the optical-pump/electron-probe UEC experiments in the transmission geometry. (c) Static diffraction pattern of a crystalline GeTe nanofilm obtained in UEC; the peaks are labeled according to the initial rhombohedral structure but also for the cubic structure of the intermediate. Several peaks associated with pure-Ge clusters are also observed and marked with a star.

has in recent years become the subject of intense debate. Both thermal[8,9] and nonthermal mechanisms[10−12] have been suggested to describe the amorphization of the crystalline phase, and various atomic-scale models[13−16] have been proposed to explain the rearrangement of the local order. The first of these was the "umbrella-flip" model,[13] which predicts, based on extended X-ray absorption fine structure measurements, a coordination change from octahedral to tetrahedral during the amorphization. Although it represents an interesting idea, recent first-principle[14−16] and reverse Monte Carlo calculations[17] proposed that no coordination change is required. The amorphization is then assisted by a large number of vacancies present in GST alloys, leading the majority of the octahedrally coordinated atoms to lose some bonds and become defective.

It follows that understanding the underlying mechanism behind the phase transition requires the direct probing of the structural evolution of the lattice with ultrafast time- and atomic-scale spatial resolutions. With optical femtosecond laser excitation and probing, dynamics of amorphization of the crystalline phase have been reported.[8−10] Because of the long wavelength of the optical probe, the individual atomic motions of lattice dynamics are not observable. Ultrafast electron diffraction provides the means, particularly in nanofilms, for such studies of structural dynamics at the spatiotemporal resolution needed, which, in this case, is important because the "information bits" are carried out by the lattice. This technique has successfully been applied in the studies of melting, phase transitions, and lattice dynamics of other materials.[18−25]

Here, we specifically investigate, using ultrafast electron crystallography (UEC) in the transmission geometry (Figure 1b), the lattice evolution of crystalline GeTe nanofilms, a prototypical PCM and the most suitable system for quantitative studies of the phase transformation because of its well-defined and characterized structure. Following a femtosecond optical excitation, we monitored the temporal behavior of the measured positions and intensities of Bragg reflections. A transient solid−solid transformation from the initial rhombohedral phase (α-GeTe) to a rocksalt-type structure (β-GeTe) is observed, a process that was found to have a speed of 1/(12 ps). Studies of the fluence dependence of both intensity and position for different Bragg reflections indicate that this phase transition is mediated by the combined effect of electronic and structural instabilities. As discussed below, the process is distinct from that of thermal heating of the lattice, which typically leads to equilibration in hundreds of picoseconds and drives the system toward the final amorphous state, provided it is excited with high enough energy (fluence) and has a high cooling rate. The spatiotemporal sampling reported here reveals the formation of a high-symmetry intermediate structure in the early stages of the amorphization process when the material is driven by an ultrafast optical excitation. These results elucidate the elementary steps defining the structural pathway and the non-concerted nature of the phase transformation in PCMs. The identification of intermediates for GeTe helps to establish the general mechanism for all GST alloys, where several structural intermediates also exist.[26,27] As such, the relative time scales of the different transient structures, and that of amorphization, will then provide the possible limit for the performance of PCMs.

RESULTS AND DISCUSSION

The details of the UEC experiments are reported in the Methods. Briefly, the sample is a 20 nm-thick free-standing crystalline GeTe film. The static diffraction pattern is representative of the rhombohedral α-phase
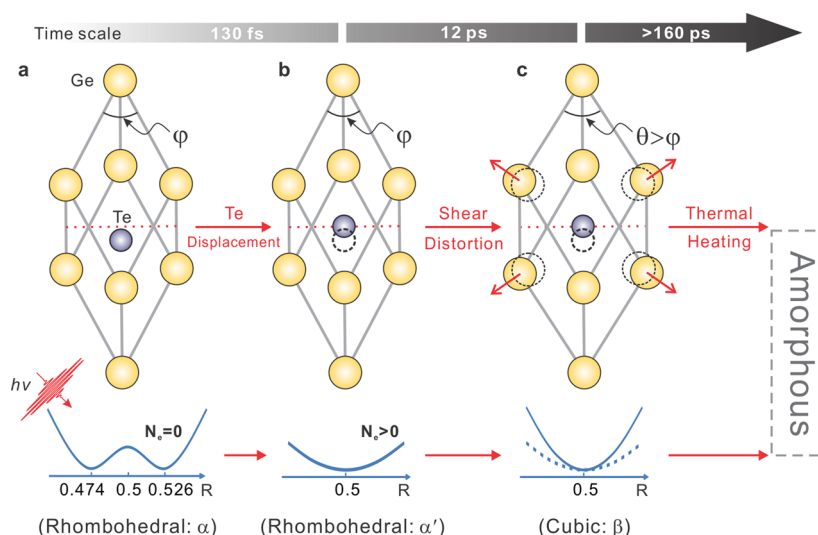
Figure 2. Structural intermediates of the phase transition. The atomic mechanism behind the transition from the initial rhombohedral structure to the final amorphous phase (from left to right). First, a movement of Te atoms takes place on the fs time scale ($\alpha \rightarrow \alpha'$), and then a shear deformation of the lattice results in the cubic structure on a time scale of 12 ps ($\alpha' \rightarrow \beta$). Finally, the thermal heating, which equilibrates in hundreds of picoseconds, creates a liquid state and leads the system toward the amorphous state, provided the fluence is high enough and the system rapidly quenches. The change of the interatomic potential associated with the different phases is also indicated; $\varphi = 57.94°$ and $\theta = 60°$ are the rhombohedral angles of the α and β phases, respectively.

(Figure 1c and Figure S1 in the Supporting Information). The structural dynamics are initiated by a 120 fs laser pulse (wavelength of 800 nm) and probed by a sub-picosecond electron pulse at variable delay times with respect to the optical excitation (Figure 1b). The temporal evolution of the diffraction pattern is measured also as a function of the excitation fluence.

Before discussing in details our observations and their implications, it is helpful to explore the possible structural transient intermediates for GeTe. This will allow us to provide a general landscape in which the mechanism behind the transition from crystalline to amorphous structures, as derived from our experiments, can be fully understood.

Structural Intermediates. A rhombohedral phase with octahedral coordination, α-GeTe, is the energetically stable structure at room temperature (Figure 2a); the double minima in the interatomic potential represent the equivalent position, below and above the dotted line, of the Te atom along the [111] direction, R (the polarization of the A_{1g} optical phonons[28]). The first structure to consider is the one involving the movement of the Te atom toward the center of the unit cell, but keeping the rhombohedral angle, φ, unchanged;[20,29] here we term it α', with the potential along R being a single well. From the α'-phase, an intermediate cubic structure (β) is possible when the angle φ increases. This rocksalt-type, cubic structure can be related to the rhombohedral one through a symmetry reduction, which is described by the instability of the electronic and structural states, and is mediated by two different deformations. The first is a 2.6% relative down displacement of the Te atoms at the center of the cubic unit

cell along the [111] direction, as given in ref 30, whereas the second is a shear deformation of the cubic cell causing the rhombohedral angle, φ, to decrease from 60° to 57.94°.[31,32] The intraunit cell atomic displacement of Te atoms is understood as a Peierls instability of the β-phase, driven by the energy minimization in the case of half-filled valence orbitals.[33-35] This Peierls distortion induces nonequally spaced atoms along the [111] direction, therefore resulting in a double-well interatomic potential with the minima deviating from the fcc lattice sites[29] (Figure 2a).

Driving the system with, *e.g.*, a laser field causes the migration toward amorphization. Recent first-principle calculations show that the cubic phase, β-GeTe, is the most energetically favorable structure under electronic excitation.[36] From an energetic point of view, the ultrafast excitation permits the accumulation of enough carriers in the conduction band, which significantly modifies the interatomic potential, with the general tendency to raise the lattice symmetry.[18,20,29,37] A transformation of the potential from a double-well to a single one (see Figure 2b) by increasing the carrier density above a threshold value is reminiscent of an inverse Peierls' distortion, which changes the symmetry of the structure.[20,29,37] It should be noted that electron–phonon coupling plays an important role, and in this case it is the optical A_{1g} distortion (in 130 fs)[20,29] that drives the lattice into the α'-structure, shown in Figure 2b, with a negligible change of the rhombohedral angle. This picture is fully consistent with one provided by our results (see below) where a transformation toward a "real" cubic structure is demonstrated.

It is worth mentioning that when the transformation occurs through a series of thermodynamic equilibrium states (such as in static thermal annealing), an order−disorder mechanism, where the system fluctuates between the two potential minima, rather than a displacive mechanism, has been proposed to take place at a structural short-range order.[38] However, in the case of the laser-driven transition discussed here, the system explores high nonequilibrium states on its potential energy surface and the electron-driven change of the interatomic potential described above is the dominant process.

Besides the electronic potential change, a simultaneous shear deformation of the unit cell is necessary to reach the full cubic symmetry. Thus, to complete the α-to-β transition, an increase of the rhombohedral angle, φ, from 57.94° to 60° is required (Figure 2c). The time scale of this process is mainly determined by the excitation of acoustic phonons[39] via anharmonic decay of optical phonons. These two distinct pathways are analogous to the two elementary processes resolved in the transformation of metal-to-insulator transition in vanadium dioxide.[18]

Equilibrium heating of the lattice is reached on a much longer time scale. Provided that high enough excitation energy is invoked, lattice thermal vibrations in the solid material drive the system toward the Lindeman limit for melting, where the fluctuations in atomic positions, relative to interatomic distances, acquire a critical value, typically 15%. A high-rate of cooling in the molten state could then generate the final amorphous state.

Diffraction along Three Directions. From the diffraction pattern in Figure 1c, we can clearly distinguish all the low Miller indices crystallographic directions in GeTe. Using the (220), (111), and (113) reflections, which exhibit the best signal-to-noise ratio, we can univocally determine the temporal evolution of the unit cell. In order to facilitate the following discussion, Miller indices of the measured Bragg reflections have been transformed from the rhombohedral reference framework into the cubic one.[31,40] As will be shown in the next section (Dynamics and Time Scales), all reflections exhibit, although with distinct amplitudes and features, an initial ultrafast dynamics (time constant of 12 ps) followed by a slower component evolving on a longer time scale (time constant of 160 ps). These values have been determined from the transient changes of both intensity and peak position for the observed Bragg reflections. The fluence dependence of the dynamics, as detailed below, can provide a clear indication of the presence of structure intermediates.

The atomic motions during the phase transformation can be probed by monitoring both the intensity, I, and the scattering vector (peak-position), s, for the observed Bragg reflections in the transmission patterns. The diffraction intensity is proportional to the

square modulus of the structure factor, F, which depends on the crystalline symmetry and the atomic displacements within the unit cell. On the other hand, lattice deformations modify lattice plane distances, and thus the corresponding scattering vectors change accordingly.

In Figure 3, the intensity change, plotted as Debye−Waller (DW) factor $W = 1/s_0^2 \log(I/I_0)$, and the peak-position change for both the ultrafast and the slow components of the measured Bragg reflections are shown as a function of the excitation fluence. In the following, we indicate with I_0 and s_0 the intensity and scattering vector before laser excitation and with $\Delta s_1/s_0 = (s_0 - s_1)/s_0$ and $\Delta s_2/s_0 = (s_1 - s_2)/s_0$ the scattering vector change for the ultrafast and slow component, respectively. Since the mean square displacement of the atoms, $<u^2>$, is proportional to the Debye−Waller factor, that is $<u^2> \propto W$, the plot of the intensity change in terms of W enables us to test whether a thermal equilibrium model is valid or not, similar to the approach used in previous works.[22,41]

For the ultrafast component (Figure 3a,c), both the intensity and the peak position display an anisotropic behavior as evident in the different Bragg reflections. The fluence dependence exhibits a threshold at 1.1 mJ/cm² with a plateau at higher values, which cannot be related to a thermal heating of the lattice. If thermal equilibration is reached, the DW factor, W, and the scattering vector change, $\Delta s/s_0$, are expected to be the same for all Bragg reflections and should exhibit a linear trend with the fluence.[42] This is contrary to the observations made for the ultrafast dynamics, although it is consistent with the results obtained for the slow-component behavior (see Figure 3b,d). Moreover, the presence of the threshold is typical of phase-transition processes in correlated systems.[18] It follows that the ultrafast component cannot be associated with a thermal-driven dynamics, and thus must be related to nonequilibrium structural changes driven by the excited carriers. It is also important to mention that we exclude a nonlinear effect in the optical absorption (such as photobleaching), since the peak power of the laser pulses at the highest fluence used (0.62 PW/m²) is well below the threshold of 2 PW/m² where nonlinearity begins to play a role.[43]

Because the structure factor, F, is sensitive to changes in lattice symmetry, the real nature of the ultrafast dynamics can be elucidated by determining its dependence on the extent of the optical excitation. For the (hkl) reflection, F is given by

$$F_{hkl}(\mathbf{r}) = \sum_j f_j \exp[-2\pi i(hkl) \cdot \mathbf{r}_j] \qquad (1)$$

where f_j are the atomic scattering factors and $\mathbf{r}_j$ defines the atomic positions. Since $I \propto |F|^2$, the DW factor is a quantitative measure of such change. When the contribution related to the optical phonons (A_{1g} and E_g)
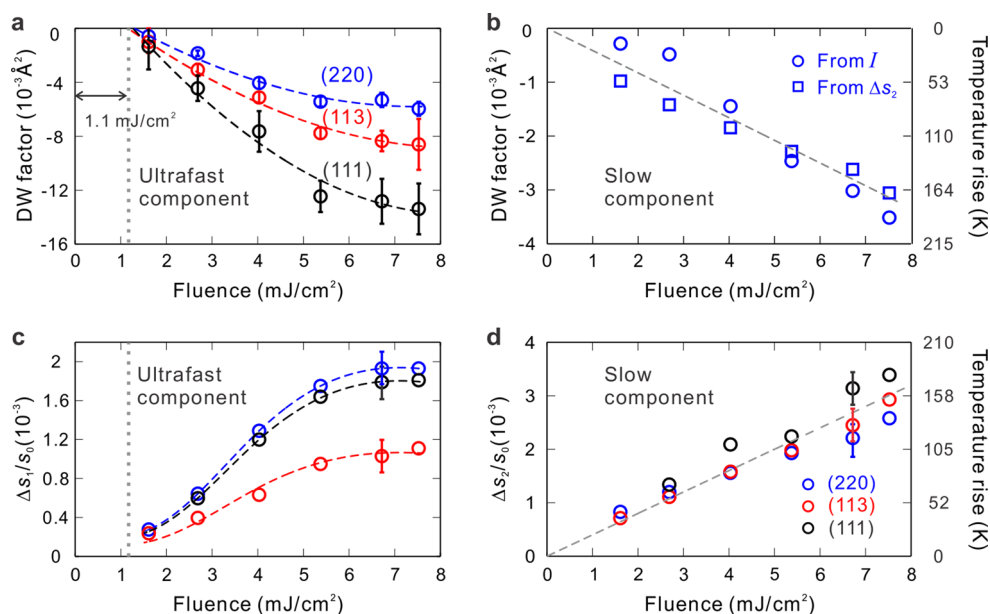
Figure 3. Fluence dependence of Bragg reflections. The intensity change, plotted as a Debye−Waller (DW) factor, $W = 1/s_0^2 \log(I/I_0)$ (panels a and b), and the peak-position change, plotted as $\Delta s/s_0$ (panels c and d), for both the ultrafast and the slow components of the measured Bragg reflections are displayed as a function of the laser fluence. The subscripts "1" and "2" are associated with the ultrafast and slow dynamics, respectively. The dashed lines are guides to the eyes. The color code is as follows: blue for (220), red for (113), and black for (111). For the ultrafast component (panels a and c), both the intensity and the peak position display an anisotropic behavior, and the fluence dependence exhibits a threshold at 1.1 mJ/cm² with a plateau at higher values. In contrast, for the slow component (panels b and d) an isotropic behavior and a linear fluence dependence are clearly visible, which is consistent with thermal heating of the lattice on this time scale (see text). The estimated temperature increase of the lattice at thermal equilibrium is shown on the right axis of panels b and d (see also the Supporting Information).

excited from the electron excitation in the initial rhombohedral phase, calculated as shown in ref 21, is subtracted from the DW factor change presented in Figure 3a, we obtain the trend shown in Figure 4a, where the nonequilibrium structural change can be isolated. Based on the selection rules of Bragg reflections for a rocksalt-type structure, the increase of the intensity for the (220) peak is consistent with the "allowed" nature of this reflection in the cubic β-phase, and the decrease for the (111) and (113) peaks is well correlated with their "quasi-forbidden" character in a cubic structure. This behavior indicates that a solid−solid transition toward the cubic phase takes place in GeTe after the ultrafast excitation.

A further confirmation of this mechanism also comes from the Bragg peak-position change. As described above, the completion of the α-to-β transition corresponds to the increase of the rhombohedral angle, φ, from 57.94° to 60°. Assuming a rigid angle change and a 0.28% reduction of the bond length, based on isotropic lattice parameter change associated with the transition measured by neutron diffraction, the shear motion responsible for the angle change can be decomposed along the [111] and [00$\bar{1}$] directions (Figure 4d). From the measured change of the peak-position for the (220), (111), and (113) reflections, we obtain the lattice strain, $\varepsilon_{(hkl)} = (\Delta d/d)_{(hkl)} = (\Delta s/s)_{(hkl)}$, along the corresponding direction. The strain components $\varepsilon^s_{(111)}$ and $\varepsilon^s_{(00\bar{1})}$ along the [111] and [00$\bar{1}$]

directions can be obtained by projecting the measured deformations, $\varepsilon_{(220)}$, $\varepsilon_{(111)}$ and $\varepsilon_{(113)}$, along these directions. At the highest fluence used (7.5 mJ/cm²), we obtain 0.6×10^{-3} and 1.1×10^{-3} for $\varepsilon^s_{(111)}$ and $\varepsilon^s_{(00\bar{1})}$, respectively (see also Figure S5a in the Supporting Information).

The strains $\varepsilon^s_{(111)}$ and $\varepsilon^s_{(00\bar{1})}$ can be used to determine, by geometrical consideration at each fluence, the change of the atomic positions, $\mathbf{r}_j$, within the unit cell. The corresponding modification of the structure factor can thus be obtained from the eq 1. These associated changes of the DW factor, which are shown in Figure 4b for the measured Bragg reflections, well reproduce the behavior obtained from the intensity change plotted in Figure 4a, thus confirming again that the ultrafast excitation is capable of promoting a transformation toward the cubic phase.

With the same geometric consideration, it is also straightforward to calculate the value of $\varepsilon^0_{(111)}$ and $\varepsilon^0_{(00\bar{1})}$ for the structure to reach the condition $\varphi = 60°$ with a simultaneous isotropic contraction of the bond length. These are 0.6×10^{-2} and 1.2×10^{-2}, respectively. However, considering the propagation of the laser pulses at 800 nm in α-GeTe, we calculated from the absorption spectra[34] a penetration depth of 14 nm (1/e), thus only the top layers of the film will be excited with sufficient carrier density to transform α into the β phase. The kinetics of the transition is straightforward to solve (see below and Supporting Information) and
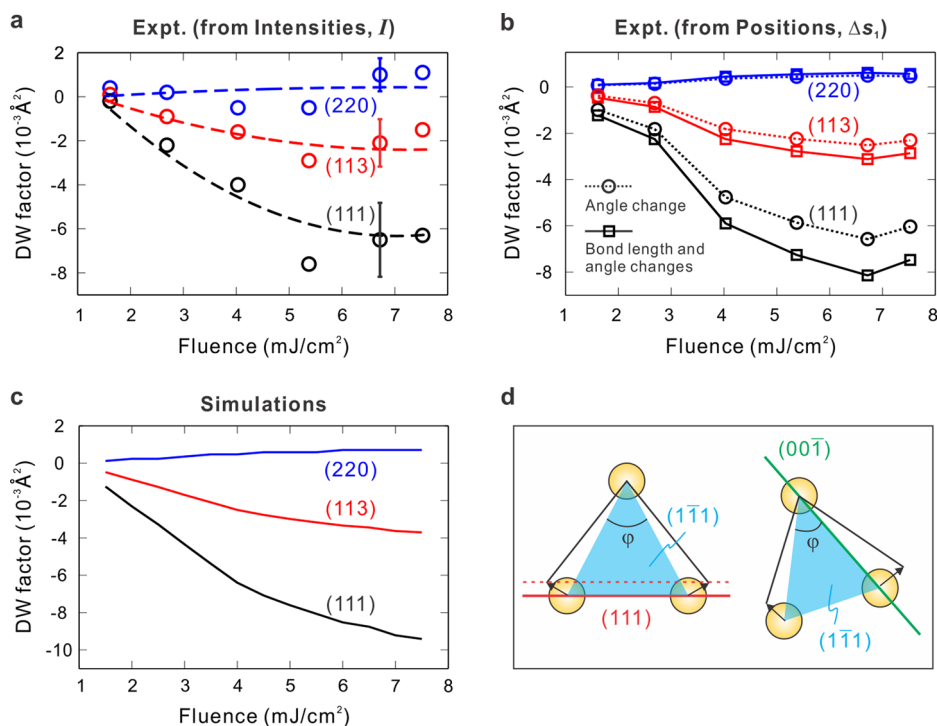
Figure 4. Phase transition and structure factor change with fluence. (a) Debye−Waller (DW) factor for the observed Bragg reflections as a function of the laser fluence, obtained from the intensity change of the ultrafast component when the contribution related to the excited optical phonons is removed. The dashed lines are guides to the eyes. **(b)** Fluence dependence of the DW factor obtained from the structure factor change when the lattice strains associated with the shear motion (increase of rhombohedral angle) and the bond length reduction, $\varepsilon^s_{(111)}$ and $\varepsilon^s_{(00\bar{1})}$, are used to determine the change of the atomic positions within the unit cell. The values of $\varepsilon^s_{(111)}$ and $\varepsilon^s_{(00\bar{1})}$ have been obtained by projecting the measured deformations, $\varepsilon_{(220)} = (\Delta s/s)_{(220)}$, $\varepsilon_{(111)} = (\Delta s/s)_{(111)}$, and $\varepsilon_{(113)} = (\Delta s/s)_{(113)}$, along the [111] and [00$\bar{1}$] directions. The dotted lines represent the variation of the structure factor when only the change of the rhombohedral angle is considered, whereas the solid lines indicate the case where both angle and bond length changes are taken into account. **(c)** Fluence dependence of the DW factor obtained from the structure factor change calculated for the α-to-β transformation using simple geometric considerations and the kinetic rates model described in the text and the Supporting Information. **(d)** Representation of the atomic motions along the [111] and [00$\bar{1}$] directions induced by the shear deformation that transforms the lattice into a cubic structure. In panels a and b, "Expt." stands for experimental. For all panels, the color code is as follows: blue for (220), red for (113), and black for (111).

gives the percentage P_β of the transformed unit cells; for example, at a fluence of 7.5 mJ/cm^2 the percentage $P_\beta = 13\%$ was obtained. The effective strain can thus be obtained: $\varepsilon^s_{(hkl)} = \varepsilon^0_{(hkl)} P_\beta$, giving the values of 0.7×10^{-3} and 1.5×10^{-3} at 7.5 mJ/cm^2 for the [111] and [00$\bar{1}$] directions, respectively (see also Figure S5b, Supporting Information), in good agreement with the experimental results. Combining eq 1 and the kinetics (for P_β), the fluence dependence of the structure factor change associated with the α-to-β transition was calculated. The trend obtained for the DW factor, plotted in Figure 4c, exhibits a satisfactory agreement with the experimental results and further confirms the transition toward the cubic phase. Moreover, the increase of the volume fraction of the formed β-phase with increasing fluence is also at the origin of the fluence-dependent behavior for $\Delta s_1/s_0$, shown in Figure 3c.

Dynamics and Time Scales. The observed transients for the Bragg reflections studied provide the rates of the elementary steps involved. In Figure 5a we present the change of the scattering vector for the (220) reflection as a function of time; similar results were obtained for the (113) and (111). The peak-position change exhibits

an initial ultrafast drop, then a plateau behavior for time delays between 20 and 30 ps, followed by a slow decay on a longer time scale. The observation of a plateau suggests that competing dynamical channels are involved in the overall process of the transformation.[18,44] Two characteristic time constants were determined by multiexponential curve fitting: 11.8 ± 1.2 ps for the ultrafast component, and 160 ± 39 ps for the slow one. The transient change of the diffraction intensity taken at long times also exhibits similar behavior. In Figure 5c we show the results for the (220), (111), and (113) Bragg peaks at times up to 200 ps. All reflections exhibit the initial ultrafast decay with a time constant of 11.6 ± 2.4 ps, followed by the slower dynamics. The measured time constant of about 12 ps correlates well with typical values for the excitation of acoustic phonons[22] and is consistent with a picture where acoustic modes mediate the shear deformation of the unit cell that drives the α-to-β transition.[39]

The transient behavior on the longer time scale reveals another dimension of structural dynamics. Given the heat diffusion coefficient in GeTe of 2.6×10^{-2} cm^2/s (see the Supporting Information)
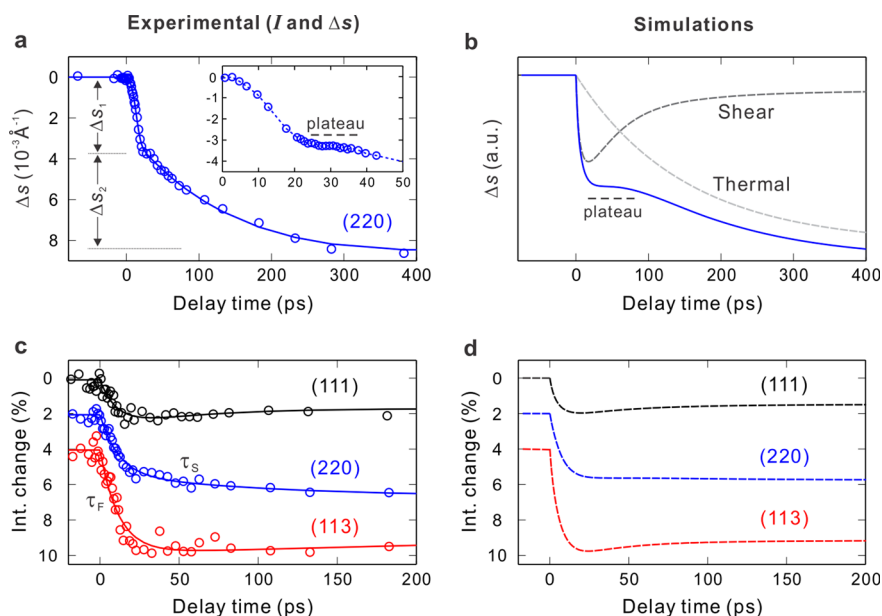
Figure 5. Dynamics and time scale. (a) Transient change of the scattering vector, $\Delta s = s_0 - s$, for the (220) peak at 4 mJ/cm^2. Δs_1 and Δs_2 represent the amplitude of the ultrafast and slow component, respectively. The inset depicts in more detail the early time region with the plateau being robust in the time region of 20−30 ps. The solid line is the exponentials best fit of the experimental data, from which two time constants are determined: 11.8 ± 1.2 ps for the ultrafast component and 160 ± 39 ps for the slow one. (b) Simulated transient change of Δs (blue solid line) from the kinetic rates model, showing also the presence of a plateau as observed experimentally. The curve is generated by the combined contribution of the shear transformation and the thermal expansion (gray dashed lines); see the text and Supporting Information for further details. (c) Experimental transient behavior of the diffraction intensity for the different observed Bragg reflections at 4 mJ/cm^2. The time constants of 11.6 ± 2.44 ps and 128.7 ± 19.7 ps are characteristic of the ultrafast and slow dynamics, respectively. (d) Simulated temporal changes of the diffraction intensity for the studied reflections. Note that for both intensity and peak position changes no further modification with respect to the trend shown in panels a and c is observed up to 1 ns. For panels a, c, and d, the color code is as follows: blue for (220), red for (113), and black for (111).

and the sample thickness of 20 nm, the heat conduction within the sample must occur in ∼150 ps, in close agreement with the time constant of 160 ps for the slow component of the peak-position change. As importantly, this slow component, as shown in Figure 3d, exhibits a linear fluence dependence, for all reflections, which is typical of a thermal heating process induced by laser excitation.[45]

To quantify the structural evolution, we developed an analytical model and simulated the lattice dynamics as a function of the delay time and excitation fluence; the details are given in the Supporting Information. The kinetics of the phase transition is described using a rate-equation approach, from which the transition probability can be obtained. A fully reversible and sequential transformation from α to β has been assumed on the time scale studied, and the rate-constants are dependent on the excited carrier density, whose dynamics also includes nonradiative recombination processes. The lattice heating under the laser excitation is obtained within the framework of the two-temperature model,[46] where energy transfer to the thermal bath via the β phase is also included

$$Th \leftpartial \alpha \rightleftharpoons \alpha' \rightleftharpoons \beta \rightpartial Th$$

where Th is the thermal bath (see also Figure S2, Supporting Information).

In parts b and d of Figure 5 we show the results of the simulations for the peak-position and intensity changes, respectively. A satisfactory agreement with the experimental results is obtained, especially when we note that the simulations not only reproduce the rates involved but also the plateau occurring in the peak position change. As evident in the intensity change (Figure 5d), the slow component is determined by the interplay of different processes: (i) the change of the structure factor (positive for the (220) and negative for (111) and (113), see also simulations in Figure S4, Supporting Information) and (ii) the thermal heating of the lattice, which equilibrates in 160 ps. The recovery of the lattice toward the initial α-phase, which is mediated by nonradiative carrier recombination occurring in hundreds of ps in GeTe,[47] is capable of relaxing the electronic system toward its initial equilibrium state. The restoring of the α-phase also corresponds to the removal of shear deformation of the unit cell, leading to a decrease of Δs, which combined with the thermal expansion of the lattice, increase of Δs, generates the observed plateau behavior (Figure 5b).

A final point is worth discussing: the laser-induced thermal heat of the α-to-β transition can be excluded. At the highest fluence used, the temperature rise, as extracted from intensity and peak-position change at long delay times (∼400 ps, when thermal equilibrium is

reached), is only 160 K (see Figure 3b and 3d). This value is much smaller than the value of 400 K necessary to thermally induce the transformation to β[30] and also smaller than the value that would be calculated if all energy absorbed by the GeTe nanofilm is converted into heat (see the Supporting Information). Other related points of this aspect are the optical pump—probe experiments in ref 9, where the authors reported that the fluence required for amorphization to be 78 mJ/cm^2, an order of magnitude higher than the value (7 mJ/cm^2) that it is obtained from the thermal properties of the material (see above and the Supporting Information) for femtosecond excitation. This is, once again, consistent with a nonthermal pathway where intermediate barriers are involved.

CONCLUSIONS

Implications on the Performance of PCMs. In summary, the spatiotemporal investigation of the structural dynamics in crystalline GeTe reveals the transient structure and relevant atomic motions involved in the phase transition mechanism following an ultrafast excitation. A nonthermal solid—solid transformation occurs in 12 ps, driving the initial rhombohedral phase toward a rocksalt-type structure, which is a precursor of the final amorphous state. The process is mediated by a shear deformation of the unit cell whose time scale is determined by selective excitation of acoustic phonons. On a much longer time scale, hundreds of picoseconds depending on the film thickness, thermal equilibrium is reached. This equilibration drives the system toward the final amorphous state, provided it is excited with high enough energy (fluence) and is rapidly quenched. Both thermal and nonthermal processes are distinct in their behavior from the change of Bragg reflections with time and their dependence on the fluence.

The ultrafast diffraction measurements reported here demonstrate the ability to disentangle the nature of the atomic motions during the phase transition and provide a more general picture for PCMs. In GST alloys, different atomic structures with similar energy are possible. In particular, the structure with the lowest energy is often characterized by an octahedral coordination where local distortions can be significant.[34,35]

By establishing the time scale for the different transient structures, and knowing that of amorphization, the ultimate performance for the recording speed of PCMs can be derived. For GeTe, the bottleneck in the amorphization process is represented by the long thermal annealing (hundreds of ps), starting from the β phase. However, for the $Ge_2Sb_2Te_5$ alloy the photo-induced amorphization only takes few ps,[48] and thus a possible solid—solid transformation between two metastable crystalline phases (cubic and hexagonal[26] in this case), similar to the behavior observed here, may play a significant role in determining the limit for the performance of $Ge_2Sb_2Te_5$-based devices.

METHODS

Sample Growth. The investigated crystalline samples were obtained using the following procedure. First, amorphous GeTe films were grown by magnetron sputtering from a stoichiometric GeTe target on a freshly cleaved NaCl substrate. The base pressure in the vacuum chamber during operation was 7×10^{-5} Pa, and an argon plasma (Ar partial pressure of 0.6 Pa) was used for the sputtering. The deposited film thickness was 20 nm as measured by a quartz-crystal thickness monitor. The as-deposited films were then transferred on 1000-mesh copper grids (TedPella) by delamination in deionized water. The crystallization of the amorphous films was obtained by annealing at relatively low vacuum ($\sim 10^{-2}$ Torr) using a GSL-1700x tube furnace. The annealing temperature of 350 °C was reached at an initial heating rate of 10 °C/min and held for 10 min, after which the sample was left to naturally cool down to room temperature. It is reasonable to assume that the film thickness did not change significantly during the crystallization process, and a nominal thickness of 20 nm is retained for the crystalline films.

It is worth mentioning that GeTe has been shown to be particularly sensitive to the annealing temperature.[49] In order to verify that no chemical change was induced by the annealing, we measured the composition of the films by electron probe microanalysis using the JEOL JXA-8200 microprobe. We determined the composition of the alloy, 47:53 (Ge:Te), which is close to its stoichiometric value of 50:50, and similar to that reported in previous studies (46:54 in ref 9). This also indicates that oxidation within the volume of the sample is negligible, and the possible formation of monolayer oxide at the sample surface,[50] as induced by postannealing air exposure, does not play a significant role because of the transmission geometry of the experiment (see below and Figure 1b). The diffraction pattern, reported in Figure 1c, shows the presence of several additional peaks that are associated with pure-Ge clusters. This is typical of a crystallization process performed by annealing and is consistent with the exhaustive investigation given in refs 40 and 51. Nevertheless, the spatial density of these Ge clusters is generally very low so that the effect on the measured structural dynamics is negligible.

UEC Experiments. The UEC setup has been described in detail in ref 45. Briefly, a laser-pump/electron-probe scheme is adopted, working in the stroboscopic mode with a variable delay time between the pump and probe pulses. Femtosecond laser pulses with a duration of 120 fs and a central wavelength of 800 nm are generated from a Ti:sapphire amplifier at the repetition rate of 1 kHz. The laser beam is divided by a beam splitter into two portions: one is the pump beam, used to initiate the dynamics and focused on the sample with a *p*-polarization and a 45° angle with respect to its normal (the spot size on the sample is 1.6 × 1.1 mm^2); the other beam portion is frequency-tripled *via* third harmonic generation creating a 266 nm UV beam. The UV beam is guided to a LaB$_6$ cathode of the photoelectron gun (Kimball Physics, Inc.) in order to generate a pulsed electron beam, which is accelerated to 30 keV and then focused in normal incidence on the sample (the spot size is 131 × 82 μm^2). Since the spot size on the sample surface for the electron beam is much smaller than that of the pump laser beam, a homogeneous excitation is guaranteed in the region probed by the electrons within a plane parallel to the surface.

In order to minimize space-charge effects, an electron pulse containing only ~360 electrons was generated, giving a pulse duration shorter than 1 ps.[52] Even taking into account the velocity mismatch[53] between electrons and photons and the

experimental geometry, the temporal resolution of the measurement is still better than 1 ps. The relative delay time between laser-pump and electron-probe is controlled by a linear delay stage inserted into the optical path of the pump beam. The diffraction patterns obtained from electron scatterings of the sample are recorded on a MCP/phosphor screen/CCD assembly, which is working in the gate mode. To obtain a good signal-to-noise ratio, more than 200 temporal scans were acquired, and in each scan every diffraction pattern was averaged over 20,000 reproducible events. At the laser fluence used in this work, the sample recovers to its initial state in less than 1 ms, before the next pump pulse arrives. In fact, no accumulated modifications or damage have been observed after several days of measurements, as confirmed by the lack of long-term changes of the diffraction pattern acquired before the laser excitation.

The diffraction pattern of crystalline GeTe nanofilms in the transmission geometry consists of Debye—Scherrer rings; this ring pattern represents averaging over crystalline domains in the range studied (grain size ∼20 nm). The pattern shown in Figure 1a is measured on thermal-annealed GeTe, performed as described above, and is representative of the rhombohedral α phase.[31] This is confirmed by the splitting of (111) and (1$\bar{1}\bar{1}$) peaks in static diffraction, as clearly visible in Figure S1 (Supporting Information), which is related to local lattice distortion stabilizing the α phase; in a perfect cubic system these two peaks would have the same scattering vector. When a fs-laser is used to crystallize the as-deposited amorphous films, instead of thermal-annealing, a similar diffraction pattern is obtained (see Figure S1, Supporting Information), attesting the relevance of the rhombohedral phase in all laser-based technological applications.

In order to facilitate the discussion, the Miller indices of the measured Bragg reflections were transformed from the rhombohedral reference framework into the cubic one: specifically, the (003), (01$\bar{4}$), and (015) Bragg reflections in the rhombohedral system correspond to the (111), (220), and (113) peaks in the cubic framework, respectively. By azimuthally averaging the two-dimensional pattern, a one-dimensional rocking curve as a function of the scattering vector can be obtained. Here, a Hough transform was used to trace the ring center of each pattern as a function of the delay time, so that any drift of the electron beam could be compensated for. To quantitatively study the dynamics, the region of interest within the rocking curve was fitted using multiple Lorentzian functions and a linear background, from which the position and the intensity of the observed diffraction peaks were carefully determined. We note that transient electric field (TEF)[54] effect in this geometry is calculated to give 13 μrad at the highest fluence of 7.5 mJ/cm^2. This gives rise to a change in Bragg peak position of 0.7×10^{-3}, a 3-fold smaller than the observed experimental change of 2×10^{-3}.

As a final comment, it is worth mentioning that coherent harmonic strain waves can be created along the direction normal to the sample surface due to the laser excitation. However, in the UEC measurements made here, the free-standing configuration of investigated films and the transmission geometry in normal incidence, where the scattering vector of the electrons is perpendicular to the polarization vector of the wave, make the contribution of this strain waves negligible in the observed transients.

Conflict of Interest: The authors declare no competing financial interest.

Supporting Information Available: Further details on sample preparation, the analytical description of rate equations and modified two temperature model, structure factor calculations, and quantitative determination of lattice strain associated with the phase transition. The Supporting Information is available free of charge on the ACS Publications website at DOI: 10.1021/acsnano.5b01965.

REFERENCES AND NOTES

1. Siegrist, T.; Merkelbach, P.; Wuttig, M. Phase Change Materials: Challenges on the Path to a Universal Storage Device. *Annu. Rev. Condens. Matter Phys.* **2012**, *3*, 215–237.

2. Raoux, S.; Welnic, W.; Ielmini, D. Phase Change Materials and Their Application to Nonvolatile Memories. *Chem. Rev.* **2010**, *110*, 240–267.

3. Wuttig, M.; Yamada, N. Phase-Change Materials for Rewriteable Data Storage. *Nat. Mater.* **2007**, *6*, 824–832.

4. Loke, D.; Lee, T. H.; Wang, W. J.; Shi, L. P.; Zhao, R.; Yeo, Y. C.; Chong, T. C.; Elliott, S. R. Breaking the Speed Limits of Phase-Change Memory. *Science* **2012**, *336*, 1566–1569.

5. Xiong, F.; Liao, A. D.; Estrada, D.; Pop, E. Low-Power Switching of Phase-Change Materials with Carbon Nanotube Electrodes. *Science* **2011**, *332*, 568–570.

6. Hamann, H. F.; O'Boyle, M.; Martin, Y. C.; Rooks, M.; Wickramasinghe, K. Ultra-High-Density Phase-Change Storage and Memory. *Nat. Mater.* **2006**, *5*, 383–387.

7. Huang, Y. L.; Huang, C. W.; Chen, J. Y.; Ting, Y. H.; Lu, K. C.; Chueh, Y. L.; Wu, W. W. Dynamic Observation of Phase Transformation Behaviors in Indium(III) Selenide Nanowire Based Phase Change Memory. *ACS Nano* **2014**, *8*, 9457–9462.

8. Siegel, J.; Gawelda, W.; Puerto, D.; Dorronsoro, C.; Solis, J.; Afonso, C. N.; de Sande, J. C. G.; Bez, R.; Pirovano, A.; Wiemer, C. Amorphization Dynamics of Ge$_2$Sb$_2$Te$_5$ Films upon Nano- and Femtosecond Laser Pulse Irradiation. *J. Appl. Phys.* **2008**, *103*, 023516.

9. Gawelda, W.; Siegel, J.; Afonso, C. N.; Plausinaitiene, V.; Abrutis, A.; Wiemer, C. Dynamics of Laser-Induced Phase Switching in GeTe Films. *J. Appl. Phys.* **2011**, *109*, 123102.

10. Takeda, J.; Oba, W.; Minami, Y.; Saiki, T.; Katayama, I. Ultrafast Crystalline-to-Amorphous Phase Transition in Ge$_2$Sb$_2$Te$_5$ Chalcogenide Alloy Thin Film Using Single-Shot Imaging Spectroscopy. *Appl. Phys. Lett.* **2014**, *104*, 261903.

11. Fons, P.; Osawa, H.; Kolobov, A. V.; Fukaya, T.; Suzuki, M.; Uruga, T.; Kawamura, N.; Tanida, H.; Tominaga, J. Photo-assisted Amorphization of the Phase-Change Memory Alloy Ge$_2$Sb$_2$Te$_5$. *Phys. Rev. B* **2010**, *82*, 041203.

12. Huang, D. Q.; Miao, X. S.; Li, Z.; Sheng, J. J.; Sun, J. J.; Peng, J. H.; Wang, J. H.; Chen, Y.; Long, X. M. Nonthermal Phase Transition in Phase Change Memory Cells Induced by Picosecond Electric Pulse. *Appl. Phys. Lett.* **2011**, *98*, 242106.

13. Kolobov, A. V.; Fons, P.; Frenkel, A. I.; Ankudinov, A. L.; Tominaga, J.; Uruga, T. Understanding the Phase-Change Mechanism of Rewritable Optical Media. *Nat. Mater.* **2004**, *3*, 703–708.

14. Akola, J.; Jones, R. O. Structural Phase Transitions on the Nanoscale: The Crucial Pattern in the Phase-Change Materials Ge$_2$Sb$_2$Te$_5$ and GeTe. *Phys. Rev. B* **2007**, *76*, 235201.

15. Huang, B.; Robertson, J. Bonding Origin of Optical Contrast in Phase-Change Memory Materials. *Phys. Rev. B* **2010**, *81*, 081204.

16. Mazzarello, R.; Caravati, S.; Angioletti-Uberti, S.; Bernasconi, M.; Parrinello, M. Signature of Tetrahedral Ge in the Raman Spectrum of Amorphous Phase-Change Materials. *Phys. Rev. Lett.* **2010**, *104*, 085503.

17. Lang, C.; Song, S. A.; Manh, D. N.; Cockayne, D. J. H. Building Blocks of Amorphous Ge$_2$Sb$_2$Te$_5$. *Phys. Rev. B* **2007**, *76*, 054101.

18. Baum, P.; Yang, D. S.; Zewail, A. H. 4D Visualization of Transitional Structures in Phase Transformations by Electron Diffraction. *Science* **2007**, *318*, 788–792.

19. Gedik, N.; Yang, D. S.; Logvenov, G.; Bozovic, I.; Zewail, A. H. Nonequilibrium Phase Transitions in Cuprates Observed by Ultrafast Electron Crystallography. *Science* **2007**, *316*, 425–429.

20. Sciaini, G.; Harb, M.; Kruglik, S. G.; Payer, T.; Hebeisen, C. T.; Heringdorf, F. J. M. Z.; Yamaguchi, M.; Hoegen, M. H. V.; Ernstorfer, R.; Miller, R. J. D. Electronic Acceleration of Atomic Motions and Disordering in Bismuth. *Nature* **2009**, *458*, 56–60.

21. Schafer, S.; Liang, W. X.; Zewail, A. H. Primary Structural Dynamics in Graphite. *New J. Phys.* **2011**, *13*, 063030.

22. Vanacore, G. M.; Hu, J.; Liang, W.; Bietti, S.; Sanguinetti, S.; Zewail, A. H. Diffraction of Quantum Dots Reveals Nanoscale Ultrafast Energy Localization. *Nano Lett.* **2014**, *14*, 6148–6154.

23. Morrison, V. R.; Chatelain, R. P.; Tiwari, K. L.; Hendaoui, A.; Bruhacs, A.; Chaker, M.; Siwick, B. J. A Photoinduced Metal-like Phase of Monoclinic VO₂ Revealed by Ultrafast Electron Diffraction. *Science* **2014**, *346*, 445–448.

24. Tao, Z. S.; Han, T. R. T.; Mahanti, S. D.; Duxbury, P. M.; Yuan, F.; Ruan, C. Y.; Wang, K.; Wu, J. Q. Decoupling of Structural and Electronic Phase Transitions in VO₂. *Phys. Rev. Lett.* **2012**, *109*, 166406.

25. Zewail, A. H.; Thomas, J. M. *4D Electron Microscopy: Imaging in Space and Time*; Imperial College Press: London, 2010.

26. Raoux, S.; Jordan-Sweet, J. L.; Kellock, A. J. Crystallization Properties of Ultrathin Phase Change Films. *J. Appl. Phys.* **2008**, *103*, 114310.

27. Matsunaga, T.; Yamada, N. Structural Investigation of GeSb₂Te₄: A High-Speed Phase-Change Material. *Phys. Rev. B* **2004**, *69*, 104111.

28. Steigmei, E. F.; Harbeke, G. Soft Phonon Mode and Ferroelectricity in GeTe. *Solid State Commun.* **1970**, *8*, 1275–1279.

29. Fritz, D. M.; Reis, D. A.; Adams, B.; Akre, R. A.; Arthur, J.; Blome, C.; Bucksbaum, P. H.; Cavalieri, A. L.; Engemann, S.; Fahy, S.; et al. Ultrafast Bond Softening in Bismuth: Mapping a Solid's Interatomic Potential with X-rays. *Science* **2007**, *315*, 633–636.

30. Chattopadhyay, T.; Boucherle, J. X.; Vonschnering, H. G. Neutron Diffraction Study on the Structural Phase Transition in GeTe. *J. Phys. C-Solid State* **1987**, *20*, 1431–1440.

31. Goldak, J.; Barrett, C. S.; Innes, D.; Youdelis, W. Structure of Alpha GeTe. *J. Chem. Phys.* **1966**, *44*, 3323–3325.

32. Rabe, K. M.; Joannopoulos, J. D. Theory of the Structural Phase Transition of GeTe. *Phys. Rev. B* **1987**, *36*, 6631–6639.

33. Lucovsky, G.; White, R. M. Effects of Resonance Bonding on Properties of Crystalline and Amorphous Semiconductors. *Phys. Rev. B* **1973**, *8*, 660–667.

34. Shportko, K.; Kremers, S.; Woda, M.; Lencer, D.; Robertson, J.; Wuttig, M. Resonant Bonding in Crystalline Phase-Change Materials. *Nat. Mater.* **2008**, *7*, 653–658.

35. Lencer, D.; Salinga, M.; Grabowski, B.; Hickel, T.; Neugebauer, J.; Wuttig, M. A Map for Phase-Change Materials. *Nat. Mater.* **2008**, *7*, 972–977.

36. Kolobov, A. V.; Fons, P.; Tominaga, J.; Hase, M. Excitation-Assisted Disordering of GeTe and Related Solids with Resonant Bonding. *J. Phys. Chem. C* **2014**, *118*, 10248–10253.

37. Murray, E. D.; Fritz, D. M.; Wahlstrand, J. K.; Fahy, S.; Reis, D. A. Effect of Lattice Anharmonicity on High-Amplitude Phonon Dynamics in Photoexcited Bismuth. *Phys. Rev. B* **2005**, *72*, 060301.

38. Matsunaga, T.; Fons, P.; Kolobov, A. V.; Tominaga, J.; Yamada, N. The Order-Disorder Transition in GeTe: Views from Different Length-Scales. *Appl. Phys. Lett.* **2011**, *99*, 231907.

39. Volkov, B. A.; Kopaev, Y. V. Theory of Phase Transitions in Semiconductors of A₄B₆ Group. *Sov. Phys.-JETP* **1973**, *37*, 1103–1108.

40. Kim, K. H.; Kyoung, Y. K.; Lee, J. H.; Ham, Y. N.; Choi, S. J. Evolution of the Structural and Electrical Properties of GeTe under Different Annealing Conditions. *J. Electron. Mater.* **2013**, *42*, 78–82.

41. Raman, R. K.; Murdick, R. A.; Worhatch, R. J.; Murooka, Y.; Mahanti, S. D.; Han, T. R. T.; Ruan, C. Y. Electronically Driven Fragmentation of Silver Nanocrystals Revealed by Ultrafast Electron Crystallography. *Phys. Rev. Lett.* **2010**, *104*, 123401.

42. Schafer, S.; Liang, W. X.; Zewail, A. H. Structural Dynamics of Nanoscale Gold by Ultrafast Electron Crystallography. *Chem. Phys. Lett.* **2011**, *515*, 278–282.

43. Fons, P.; Rodenbach, P.; Mitrofanov, K. V.; Kolobov, A. V.; Tominaga, J.; Shayduk, R.; Giussani, A.; Calarco, R.; Hanke, M.; Riechert, H.; et al. Picosecond Strain Dynamics in Ge₂Sb₂Te₅ Monitored by Time-Resolved X-ray Diffraction. *Phys. Rev. B* **2014**, *90*, 094305.

44. Paik, D. H.; Lee, I. R.; Yang, D. S.; Baskin, J. S.; Zewail, A. H. Electrons in Finite-Sized Water Cavities: Hydration Dynamics Observed in Real Time. *Science* **2004**, *306*, 672–675.

45. Yang, D. S.; Gedik, N.; Zewail, A. H. Ultrafast Electron Crystallography. 1. Nonequilibrium Dynamics of Nanometer-Scale Structures. *J. Phys. Chem. C* **2007**, *111*, 4889–4919.

46. Anisimov, S. I.; Kapeliovich, B. L.; Perel'man, T. L. Electron Emission from Metal Surface Exposed to Ultrashort Laser Pulses. *Sov. Phys.-JETP* **1974**, *39*, 375–377.

47. Sundaram, S. K.; Mazur, E. Inducing and Probing Non-Thermal Transitions in Semiconductors Using Femtosecond Laser Pulses. *Nat. Mater.* **2002**, *1*, 217–224.

48. Waldecker, L.; Miller, T. A.; Rude, M.; Bertoni, R.; Osmond, J.; Pruneri, V.; Simpson, R.; Ernstorfer, R.; Wall, S. Decoupled Optical Response and Structural Transition in Phase Change Materials. *ArXiv.1412.0901 [cond-mat.mtrl-sci]* **2014**.

49. Choi, Y. G.; Kovalskiy, A.; Cheong, B. K.; Jain, H. Role of Local Structure in the Phase Change of Ge-Te Films. *Chem. Phys. Lett.* **2012**, *534*, 58–61.

50. Yashina, L. V.; Puttner, R.; Neudachina, V. S.; Zyubina, T. S.; Shtanov, V. I.; Poygin, M. V. X-Ray Photoelectron Studies of Clean and Oxidized a-GeTe(111) Surfaces. *J. Appl. Phys.* **2008**, *103*, 094909.

51. Kolobov, A. V.; Tominaga, J.; Fons, P.; Uruga, T. Local Structure of Crystallized GeTe Films. *Appl. Phys. Lett.* **2003**, *82*, 382–384.

52. Gahlmann, A.; Park, S. T.; Zewail, A. H. Ultrashort Electron Pulses for Diffraction, Crystallography and Microscopy: Theoretical and Experimental Resolutions. *Phys. Chem. Chem. Phys.* **2008**, *10*, 2894–2909.

53. Baum, P.; Zewail, A. H. Breaking Resolution Limits in Ultrafast Electron Diffraction and Microscopy. *Proc. Natl. Acad. Sci. U.S.A.* **2006**, *103*, 16105–16110.

54. Schafer, S.; Liang, W. X.; Zewail, A. H. Structural Dynamics and Transient Electric-Field Effects in Ultrafast Electron Diffraction from Surfaces. *Chem. Phys. Lett.* **2010**, *493*, 11–18.